

Supporting Information

Harnessing van der Waals CrPS₄ and surface oxides for non-monotonic pre-set field induced exchange bias in Fe₃GeTe₂

Aravind Puthirath Balan^{1‡*}, Aditya Kumar^{1‡}, Tanja Scholz², Zhongchong Lin³, Aga Shahee^{1†}, Shuai Fu^{4†}, Thibaud Denneulin⁵, Joseph Vas⁵, András Kovács⁵, Rafal E. Dunin-Borkowski⁵, Hai I. Wang⁴, Jinbo Yang³, Bettina V. Lotsch², Ulrich Nowak⁶, Mathias Kläui^{1,7*}

¹Institute of Physics, Johannes Gutenberg University Mainz, Staudinger Weg 7, 55128 Mainz, Germany.

²Max Planck Institute for Solid State Research, Heisenbergstraße 1, 70569 Stuttgart, Germany.

³State Key Laboratory for Artificial Microstructure and Mesoscopic Physics, School of Physics, Peking University, Beijing 100871, China.

⁴Max Planck Institute for Polymer Research Mainz, Ackermannweg 10, 55128 Mainz, Germany

⁵Ernst Ruska-Centre for Microscopy and Spectroscopy with Electrons and Peter Grünberg Institute, Forschungszentrum Jülich, 52425 Jülich, Germany

⁶Department of Physics, University of Konstanz, Universitaetsstrasse 10, 78464 Konstanz, Germany

⁷Centre for Quantum Spintronics, Department of Physics, Norwegian University of Science and Technology, 7491 Trondheim, Norway.

‡These authors contributed equally

* Correspondence to aravindputhirath@uni-mainz.de, klaeui@uni-mainz.de

Section 1 Raman Spectroscopy of Bulk Fe₃GeTe₂ and CrPS₄

Section 2 Transmission Electron Microscopy

Section 3 Atomic Force Microscopy

Section 4 STEM-EELS analysis

Section 5 XPS analysis

Section 6 Transport across a Verwey transition

Section 7 Schematic highlighting the role of ‘pre-set’ field

Section 8 Influence of the major ferrimagnetic Fe₃O₄ phase on exchange bias

Section 9 Absence of ‘pre-set field’ induced exchange bias in pristine CrPS₄/Fe₃GeTe₂ interface

Section 10 Comparison of magnitude of exchange bias as a function of various cooling fields (H_{FC}) and pre-set field (H_{PF})

Section 11 Strength of exchange bias below and above 70K

1. Raman Spectroscopy

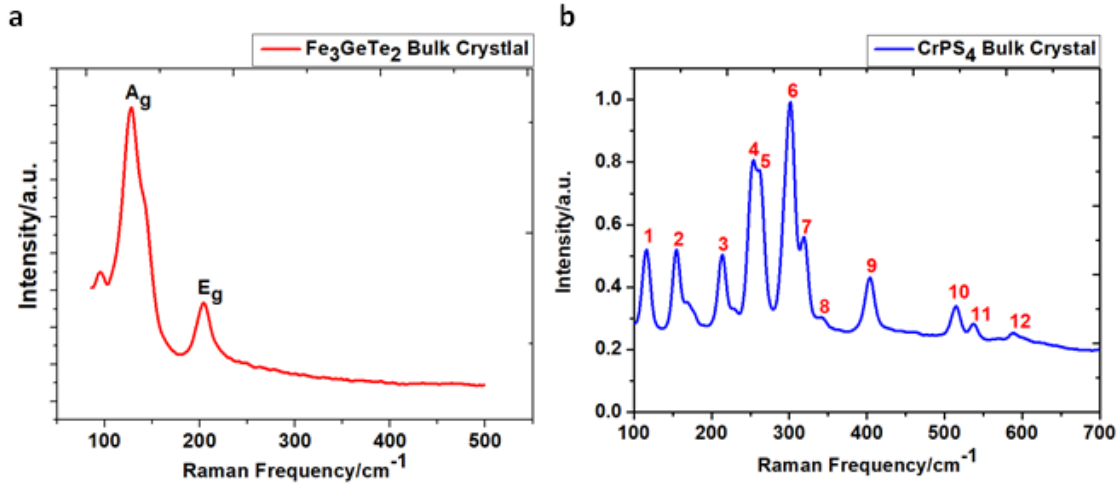


Figure S1. Raman spectra of (a) Fe₃GeTe₂ bulk crystal, and (b) CrPS₄ bulk crystal respectively.

The quality of synthesized crystals was examined by Raman spectroscopy and are summarized in *Figure S1*. All the modes obtained for both Fe₃GeTe₂ and CrPS₄ bulk crystals match well with the predicted Raman modes^{1,2}.

2. Transmission Electron Microscopy

Transmission electron microscopy (TEM) was used to examine a heterostructure composed of CrPS₄/(O-FGT)/Fe₃GeTe₂ to verify the oxide formation and composition of the oxidized Fe₃GeTe₂ flake. To induce surface oxidation, an exfoliated Fe₃GeTe₂ on Si/SiO₂ (300 nm) was subjected to annealing at 120 degrees for 1 hour under ambient conditions. Subsequently, a CrPS₄ flake was dry transferred on top to create the CrPS₄/(O-FGT)/Fe₃GeTe₂ heterostructure. Electron transparent cross-section view lamellas were prepared using a focused Ga⁺ ion beam and scanning electron microscope (FIB-SEM) FEI Helios platform. Scanning transmission electron microscopy (STEM) and energy dispersive X-ray (EDX) spectroscopy were carried out using an FEI Titan TEM equipped with a Schottky field emission gun operated at 200 kV, a CEOS probe aberration corrector, a high angle annular dark-field detector (HAADF) and a Super-X EDX detection system. Elemental maps and profiles were obtained using the Thermo Scientific Velox software. The results are summarized in *Figure S2*. Electron energy loss spectroscopy (EELS) was carried out using an Enfinium ER spectrometer from Gatan. EELS

spectra were analyzed using routines available in the Digital Micrograph software. The results are summarized in *Figure S4*.

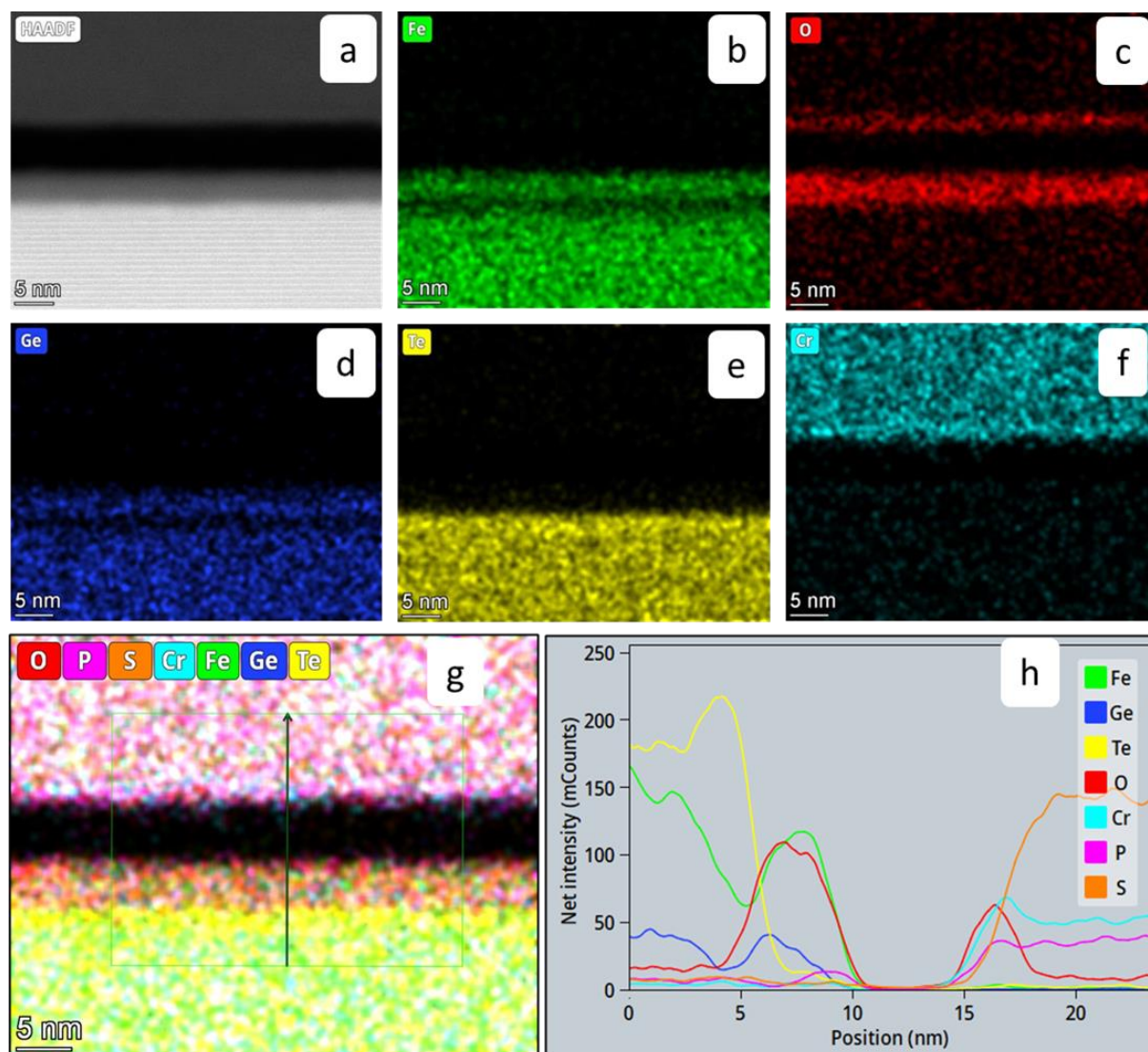


Figure S2. (a) Cross-sectional HAADF-STEM image of the interface region of an $\text{Fe}_3\text{GeTe}_2/(\text{O-FGT})/\text{CrPS}_4$ heterostructure. (b-f) Elemental maps of Fe, O, Ge, Cr obtained using EDX spectrum imaging. (g,h) Intensity profiles of the different elements along the vertical direction (h) (according to the arrow in (g)).

3. Atomic Force Microscopy

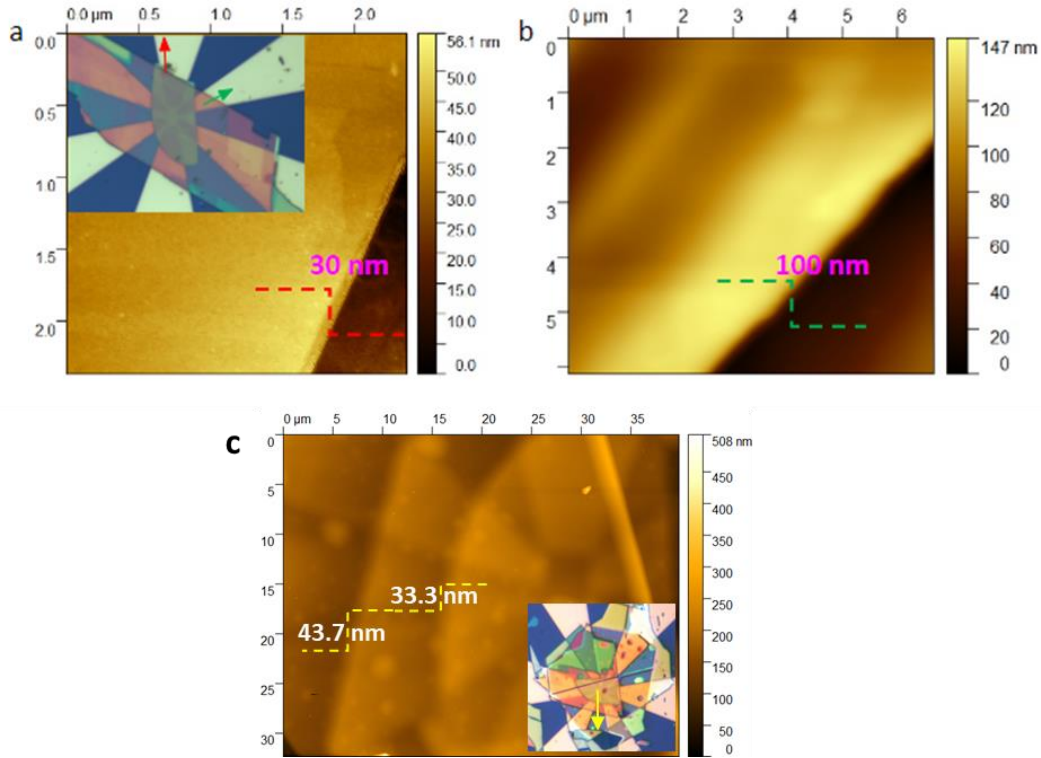


Figure S3. Atomic Force Microscope Images: Thickness of (a) Fe_3GeTe_2 flake, (b) CrPS_4 flake of the exposed device and, (c) Fe_3GeTe_2 and CrPS_4 flakes of the encapsulated device. An optical image of the respective devices is given in the inset with the AFM line profiles indicated by arrows.

The thickness of the Fe_3GeTe_2 and CrPS_4 of the exposed heterostructure as well as the encapsulated device were determined using Veeco (Bruker) 3100 Dimension Atomic Force Microscope in tapping mode. The measurement computer is connected to a NanoScope IV controller that drives atomic force microscope and the analysis is performed using Gwyddion software. The atomic force microscope images obtained are provided in *Figure S3*. The lines along which we measured the AFM line profile are marked in the optical image (*Figure S3a* and *Figure S3c* insets) with color coded arrows. The thickness obtained for Fe_3GeTe_2 (*Figure S3a*) and CrPS_4 (*Figure S3b*) for the exposed heterostructure are indicated by red and green line profiles indicating measured thickness of $30 \pm 2 \text{ nm}$ and $100 \pm 2 \text{ nm}$ respectively. Whereas, for the encapsulated device, the thickness obtained for Fe_3GeTe_2 and CrPS_4 (*Figure S3c*) as

indicated by yellow line profile are 33.3 ± 11.2 nm and 43.7 ± 9.8 nm respectively. The large error bars are because of the thick hBN layer encapsulation.

4. Cross-sectional STEM-EELS analysis: identification of pertaining oxide phases

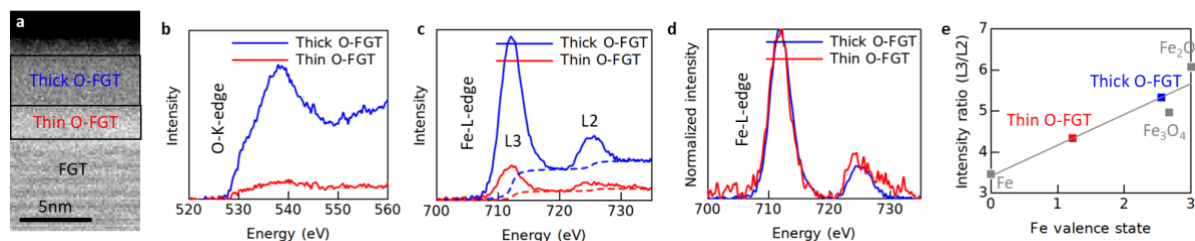


Figure S4. Oxide phases in O-FGT (a) STEM image of the surface of the FGT sample. (b) O-K-edge and (c) Fe-L-edge EELS spectra of the thick and thin oxide layers as indicated by rectangles in (a). Pre-edge background was removed using an inverse power law function. The intensity in the two regions is different because the thick O-FGT region is richer in Fe and O than the thin O-FGT layer, which is richer in Te. Dashed lines show double arctangent functions used for fitting the post-edge background. (d) Post-edge background-corrected Fe-L-edge EELS spectra. Intensities of the L3 peaks in the two regions have been normalized to show differences in the L2 peak. (e) Fe L3/L2 intensity ratios as a function of Fe valence state. Intensities were calculated by fitting the peaks with Gaussian functions. Gray line is a linear fit obtained using three reference spectra of Fe, Fe₃O₄ and Fe₂O₃. L3/L2 ratio is larger in the Fe-rich thick O-FGT compared to the thin O-FGT indicating a higher valence state.

Figure S4 shows cross-sectional STEM-EELS analysis of a FGT/O-FGT/CrPS₄ vdW heterostructure. The results suggest the presence of two types of O-FGT layers: a thicker upper layer predominantly composed of Fe₃O₄, as indicated by the L3/L2 intensity ratio, and a thinner bottom layer that may consist of FeO with a lower oxidation state.

5. X-ray photoelectron spectroscopy: identification of Fe valence states

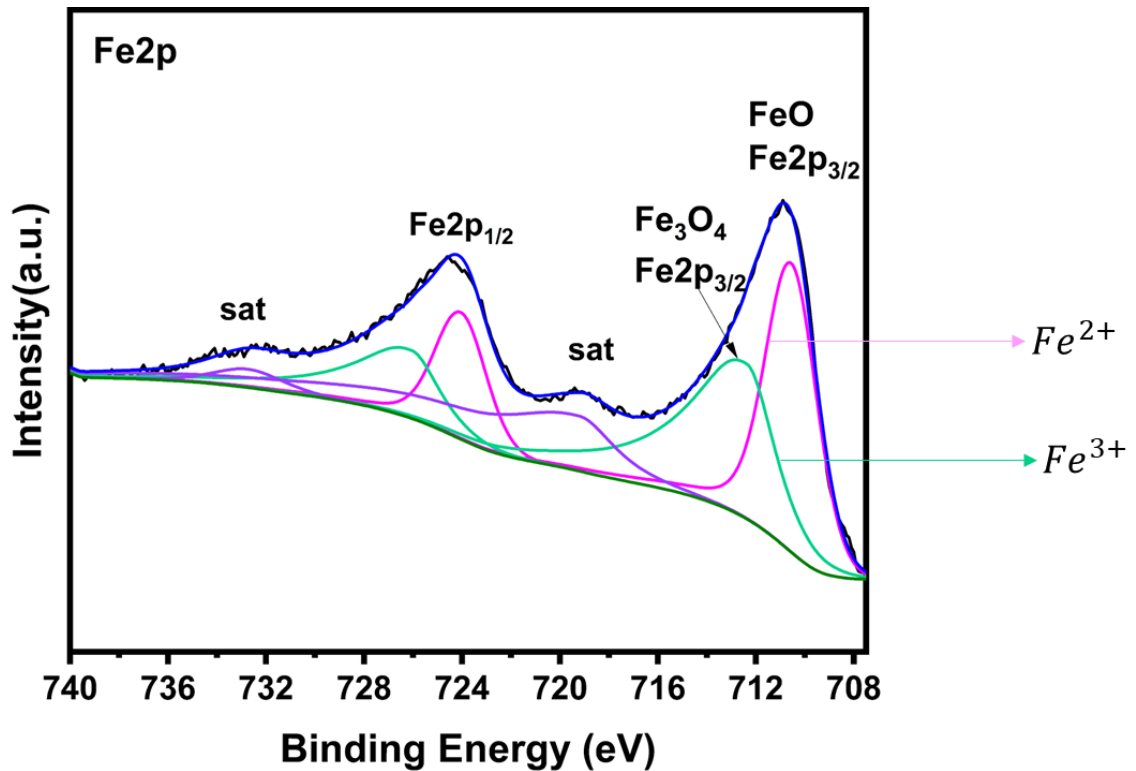


Figure S5. Fe2P spectra obtained from the oxide layer on top of an exfoliated flake. Deconvoluted Fe2P_{3/2} and Fe2P_{1/2} spectra designate Fe³⁺ (green) and Fe²⁺ (pink) valence states of iron corresponding to Fe₃O₄ or FeO.

Figure S5 shows X-ray photoelectron spectroscopy of an oxidised Fe₃GeTe₂ flake. The spectra shows evidence of presence of different valence states of iron consistent with STEM-EELS analysis.

6. Transport across a Verwey transition

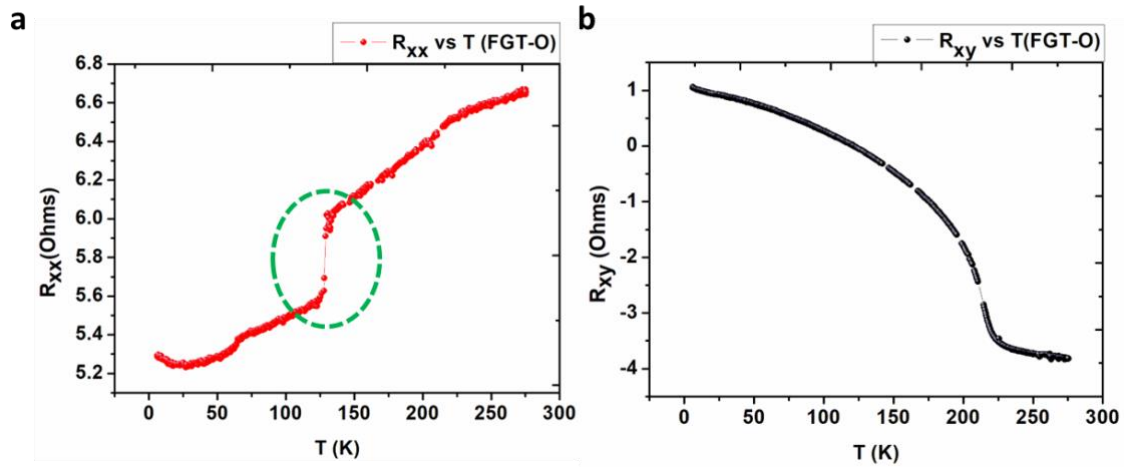


Figure S6. Transport across Verwey transition: (a) Longitudinal resistance (R_{xx}) as a function of temperature (at $\mu_0 H = 0.1 T$) highlighting (green dotted ellipse) a sudden rise characteristic of insulator to half-metallic Verwey transition in Fe_3O_4 , whereas (b) the transverse Hall resistance (R_{xy}) as a function of temperature (at $\mu_0 H = 0.1 T$) is unaffected since the ultra-thin oxide contribution could be subtle compared to bulk Fe_3GeTe_2 .

Figure S6 summarizes the longitudinal (R_{xx}) and transverse Hall resistance (R_{xy}) of an oxidized Fe_3GeTe_2 flake. Fe_3O_4 is characterized by a magneto-structural phase transition at about 80 K to 125 K which is known as Verwey transition (T_V). At this point, magnetite undergoes a phase transition from insulating monoclinic structure to a half-metallic inverse spinel cubic structure (which however is still a poor conductor)³. Here, R_{xx} (Figure S6a) has a sudden jump at around 125 K that can be corresponding to the Verwey transition (T_V) of the magnetite oxide layer. Below T_V , since the magnetite layer is in insulating monoclinic phase, the current flows only through Fe_3GeTe_2 . However, above T_V current can flow through both Fe_3GeTe_2 as well as the Fe_3O_4 layer as indicated by a sudden rise in R_{xx} at $T_V = 125 \text{ K}$. However, the oxide layer has little effect on Hall (transverse) resistance (Figure S6b).

7. Schematic highlighting the role of ‘Pre-set’ field in determining the direction of pinning.

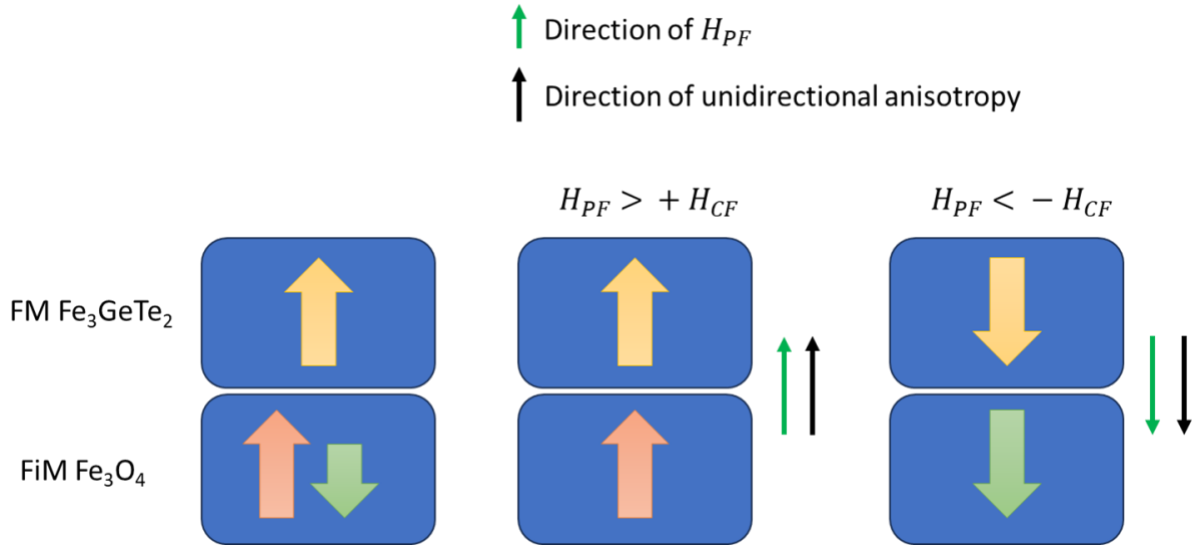


Figure S7. Schematic highlighting how ferrimagnetic Fe_3O_4 pins Fe_3GeTe_2 in the direction of the applied ‘pre-set field’ (H_{PF}). The pinning is in the direction of pre-set field which results in the hysteresis loop shifts in opposite direction.

Figure S7 shows a schematic depicting control of exchange bias by a pre-set field (H_{PF}). Applying a field larger than the critical pre-set field (H_{CF}) saturates ferrimagnetic Fe_3O_4 along the applied field direction and induces exchange bias in Fe_3GeTe_2 . Similarly, applying the field larger than H_{CF} in opposite direction saturates Fe_3O_4 in opposite direction and switches the polarity of exchange bias.

8. Influence of the major ferrimagnetic Fe₃O₄ phase on exchange bias

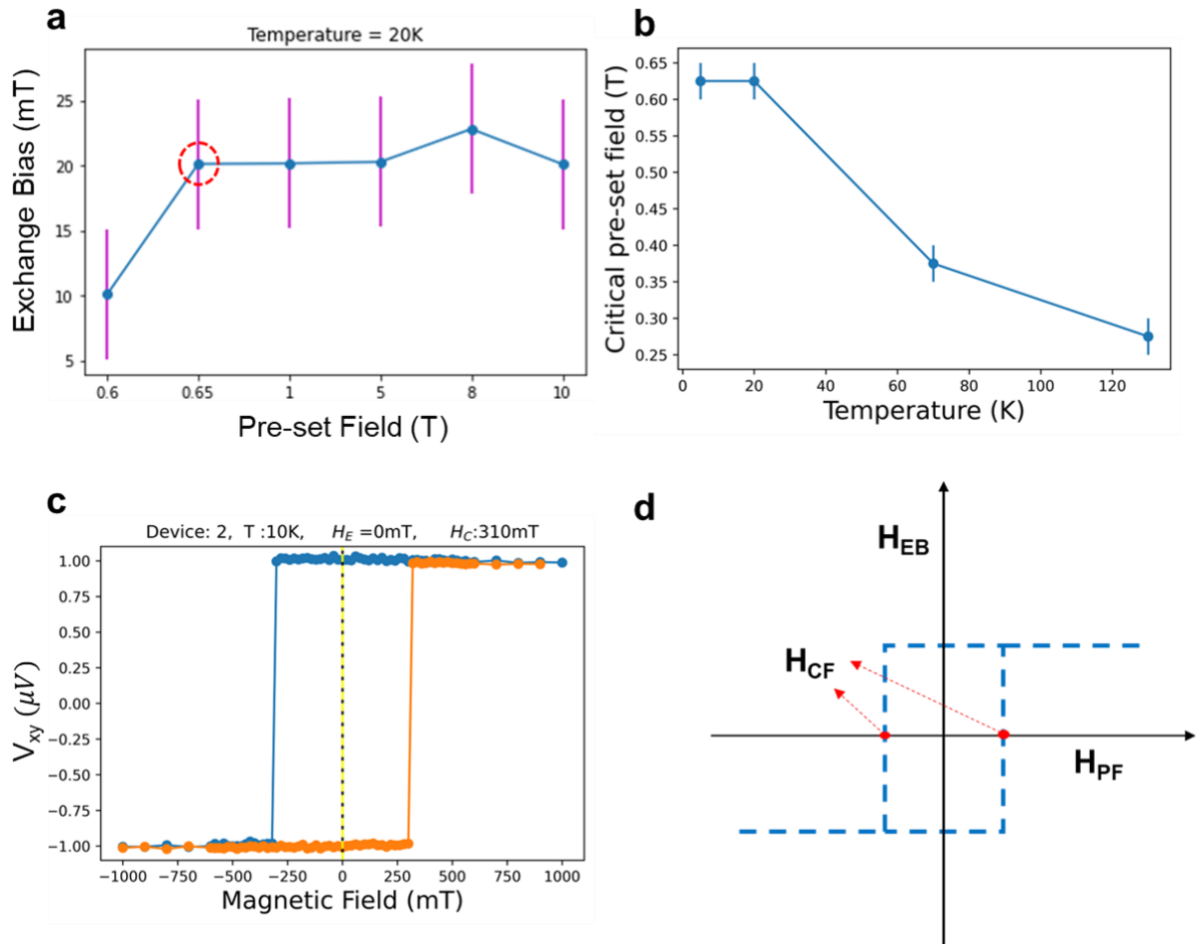


Figure S8. Influence of Ferrimagnetic Fe₃O₄ Oxide (a) The critical pre-set field (H_{CF}) determined at $T = 20$ K. (b) The variation of magnitude of H_{CF} as a function of temperature. (c) At 10 K, a sweep with a maximum field value (1 T) greater than H_{CF} (~ 600 mT) results in vanishing of EB. (d) Schematic representation of how exchange bias evolves with a pre-set field with the critical points, where EB switches direction, are marked with red dots.

Figure S8 explains how a ferrimagnetic Fe₃O₄ layer generates a pre-set field (H_{PF}) induced EB. H_{EB} was determined for different values of H_{PF} and plotted as a function of H_{PF} (*Figure S8a*). We observed that H_{EB} remains constant beyond a critical value of H_{PF} , which is termed as critical pre-set field (H_{CF}) and the magnitude of H_{CF} found to be decreasing as we increase the temperature (*Figure S8b*). Such a variation of H_{CF} as a function of temperature is similar to how

the coercive field of a ferrimagnetic Fe_3O_4 varies with temperature⁴. Moreover, after applying a $H_{PF} = \pm 1 \text{ T}$, if we use a maximum field greater than the H_{CF} while scanning the field, the exchange bias (EB) disappears. This is because there is no favored alignment for the ferrimagnetic Fe_3O_4 that establishes the pinning. [5]. In *Figure S8c*, the AHE voltage (V_{xy}) as a function of sweeping field at 20 K after applying $H_{PF} = +1 \text{ T}$ shows a symmetric hysteresis since the maximum field in positive and negative direction ($\pm 1 \text{ T}$) is greater than the H_{CF} of the Fe_3O_4 layer at 20 K ($H_{CF} \sim 0.65 \text{ T}$). Importantly, at a given temperature, we could choose the direction of the EB just by saturating the ferrimagnetic Fe_3O_4 along a preferred direction by applying a $H_{PF} > H_{CF}$ as discussed in Section 7, which is schematically demonstrated in *Figure S8d* – a plot showing how the EB (H_{EB}) varies and switches direction when $H_{PF} > H_{CF}$.

9. Absence of ‘pre-set field’ induced exchange bias in pristine $\text{CrPS}_4/\text{Fe}_3\text{GeTe}_2$ interface

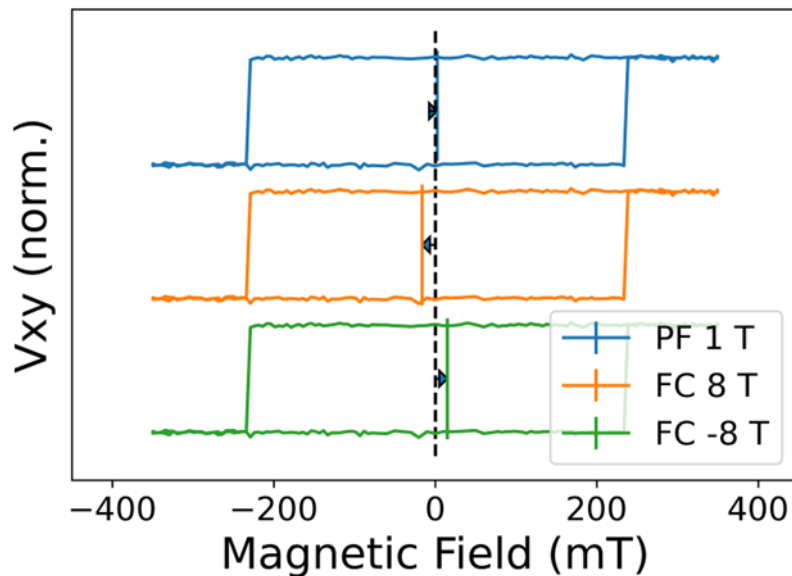


Figure S9. Absence of EB for a 1T pre-set field (blue curve), whereas finite EB for field-cooling (orange and green curves) is observed for a hBN capped $\text{CrPS}_4/\text{Fe}_3\text{GeTe}_2$ stack with pristine interface indicating effectiveness of a hBN capping layer in preventing oxidation during exposure for a short duration ($< 1 \text{ hour}$).

Figure S9 shows AHE hysteresis loops after applying 1 T pre-field and field cooling with +ve and -ve 8 T field. The plots show absence of pre-field induced exchange bias in h-BN capped $\text{Fe}_3\text{GeTe}_2/\text{CrPS}_4$ device. This evidence supports the claim that exchange bias in pristine $\text{Fe}_3\text{GeTe}_2/\text{CrPS}_4$ device does not originate from the oxide.

10. Comparison of magnitude of exchange bias as a function of various cooling fields (H_{FC}) and pre-set field (H_{PF})

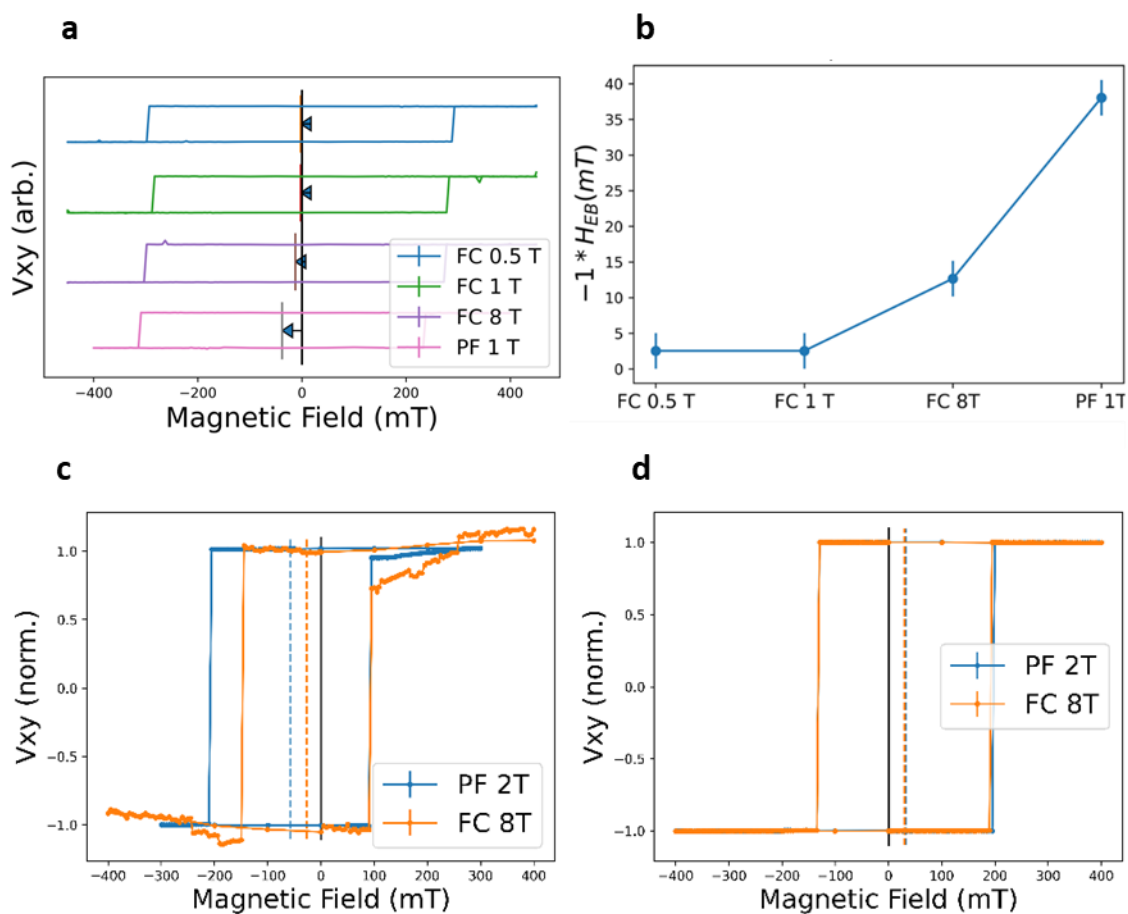


Figure S10. (a) Anomalous Hall voltage as a function of sweeping field, for the original $\text{CrPS}_4/(\text{O-FGT})/\text{Fe}_3\text{GeTe}_2$ device, preceded by field-cooling (0.5 T, 1 T and 8T) as well as 1 T pre-set field with the corresponding EB indicated by arrows; (b) Comparison of magnitude of EB calculated from Figure S10a for various cooling fields and pre-set fields; and the magnitude of EB at 10 K for field sweeps preceded by + 8T field-cooling and +2T pre-set field for a freshly prepared (c) hBN/ $\text{CrPS}_4/(\text{O-FGT})/\text{Fe}_3\text{GeTe}_2$ device, and (d) a hBN/ $(\text{O-FGT})/\text{Fe}_3\text{GeTe}_2$ device respectively.

Figure S10 elucidates the pronounced dependence of the exchange bias (EB) field on whether the measurement is preceded by conventional field-cooling or a pre-set field below 20 K, which is the blocking temperature of CrPS₄ (refer to Figure 1d). Figures S10a and S10b summarize that the exchange bias field obtained at 10 K with a 1T pre-set field is significantly larger compared to the exchange bias field obtained even with an 8 T field-cooling. This substantial reliance on the method employed to induce EB can be attributed to the distinct behavior of CrPS₄ during pre-set field application versus field-cooling. Specifically, field-cooled CrPS₄ exhibits converse effects on H_{EB} , while CrPS₄ under pre-field application does not. This observation is further experimentally validated using a freshly prepared pair of devices: hBN/CrPS₄/(O-FGT)/Fe₃GeTe₂ and hBN/(O-FGT)/Fe₃GeTe₂. The former device demonstrates a significant reduction in H_{EB} with 8 T field-cooling compared to the H_{EB} obtained with a 2 T pre-set field (Figure S10c). In contrast, the latter device shows no difference in H_{EB} for a similar set of field-cooling and pre-set field-assisted EB measurements (Figure S10d).

11. Strength of exchange bias below and above 70K

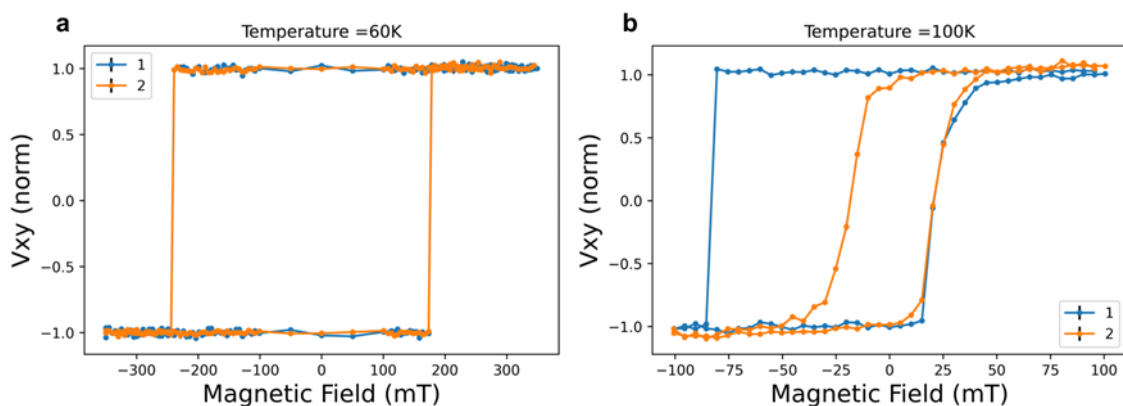


Figure S11. Training effects below and above 70 K: The exchange bias below 70 K is immune to training effect (a), however above 70 K it diminishes drastically after the first cycle (b). The significant training effect above 70 K might be due to weaker exchange coupling between Fe₃O₄ and Fe₃GeTe₂ because of in-between FeO spacer layer.

Figure S11 shows little (Figure S11a) and significant (Figure S11b) training effect for two consecutive field sweeps measured after a $H_{PF} = +1 T$ for the device with additional oxide layer at the interface. It provides a measure of the training effect of EB on either side of the minimum at $T = 70 K$ in the plot showing variation of H_{EB} as a function of temperature (Please refer main Figure 1d). 70 K is the blocking temperature of the antiferromagnetic FeO in the O-FGT above which it does not contribute to EB whereas Fe_3O_4 is the only source of pinning (please refer to the intuitive model explained in Figure 3d). However, Fe_3O_4 pins a Fe_3GeTe_2 interfacial layer through a not magnetically well-ordered spacer layer that consists of mainly FeO. Such a spacer layer can be responsible for a reduced longevity of EB and contribute to a significant training effect. Moreover, the observed asymmetry in the loop behaviour above 70 K is attributed to the difference in effective fields experienced by FM spins from the Fe_3O_4 ferrimagnetic sub-lattices while rotating through the forward and reverse direction ⁶.

References

1. Kong, X.; Berlijn, T.; Liang, L. Thickness and Spin Dependence of Raman Modes in Magnetic Layered Fe_3GeTe_2 . *Advanced Electronic Materials* **2021**, 7, 2001159.
2. Wu, H.; Chen, H. Probing the properties of lattice vibrations and surface electronic states in magnetic semiconductor CrPS4. *RSC Advances* **2019**, 9, 30655-30658.
3. Piekarcz, Przemysław; Krzysztof Parlinski; and Andrzej M. Oleś. "Mechanism of the Verwey transition in magnetite." *Physical Review Letters* **2006**, 97,156402.
4. Özdemir, Ö.; Dunlop, D. J.; & Moskowitz, B. M. Changes in remanence, coercivity and domain state at low temperature in magnetite. *Earth and Planetary Science Letters* **2002**, 194, 343-358.
5. Dho, J. Magnetic-field-induced switchable exchange bias in NiFe film on (110) Fe_3O_4 with a strong uniaxial magnetic anisotropy. *Applied Physics Letters* **2005**, 106, 202405.
6. Stamps, R. L. "Mechanisms for exchange bias." *Journal of Physics D: Applied Physics* **2000**, 33, R247.